

Beyond Mie Theory: Systematic Computation of Bulk Scattering Parameters based on Microphysical Wave Optics

YU GUO, University of California, Irvine, USA
 ADRIAN JARABO, Universidad de Zaragoza - I3A, Spain
 SHUANG ZHAO, University of California, Irvine, USA

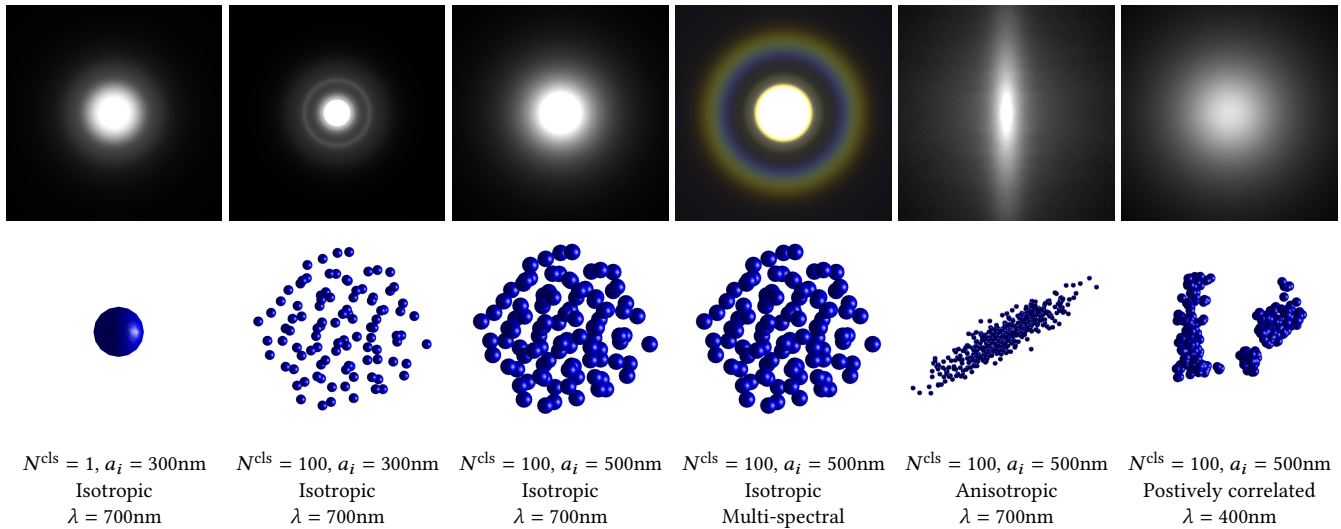


Fig. 1. We introduce a new technique to compute bulk scattering parameters (i.e., the extinction and scattering coefficients as well as the single-scattering phase function) in a systematic fashion. By considering wave optical effects and particle (scatterer) interactions at the microscopic level, our technique enjoys the generality of supporting a wide range of media (e.g., isotropic, anisotropic, and correlated). In this figure, we show renderings of thin slabs lit with a small area light from behind (top). Additionally, we show visualizations of the corresponding particle distributions (middle) as well as per-cluster particle counts N^{cls} and radii a_i (bottom).

Light scattering in participating media and translucent materials is typically modeled using the radiative transfer theory. Under the assumption of independent scattering between particles, it utilizes several bulk scattering parameters to statistically characterize light-matter interactions at the macroscale. To calculate these parameters based on microscale material properties, the Lorenz-Mie theory has been considered the gold standard. In this paper, we present a generalized framework capable of systematically and rigorously computing bulk scattering parameters beyond the far-field assumption of Lorenz-Mie theory. Our technique accounts for microscale wave-optics effects such as diffraction and interference as well as interactions between nearby particles. Our framework is general, can be plugged in any renderer supporting Lorenz-Mie scattering, and allows arbitrary packing rates and particles correlation; we demonstrate this generality by computing bulk scattering parameters for a wide range of materials, including anisotropic and correlated media.

CCS Concepts: • **Computing methodologies** → **Rendering**.

Additional Key Words and Phrases: Radiative transfer, bulk scattering parameters, wave optics

Authors' addresses: Yu Guo, guo.yu@uci.edu, University of California, Irvine, USA; Adrian Jarabo, ajarabo@unizar.es, Universidad de Zaragoza - I3A, Spain; Shuang Zhao, shz@ics.uci.edu, University of California, Irvine, USA.

1 INTRODUCTION

Participating media and translucent materials—such as marble, milk, wax, and human skin—are ubiquitous in the real world. These materials allow light to penetrate their surfaces and scatter in the interior. In computational optics and computer graphics, how light interacts with participating media and translucent materials is typically modeled using the radiative transfer theory (RTT). Under this formulation, a participating medium consists of microscopic particles (*scatterers*) randomly dispersed in some homogeneous embedding medium. After entering a translucent material, light travels in straight lines in the embedding medium and occasionally collides with a particle and gets redirected into a new direction. To capture the macroscopic behavior of light, the RTT uses a statistical description of the particles (the medium bulk parameters), namely the extinction coefficient σ_t (aka. optical density), the scattering coefficient σ_s , and the phase function f_p .

While purely phenomenological in origin, the RTT has been demonstrated a corollary of Maxwell equations, under the assumption of far-field or independent scattering [Mishchenko 2002]. Therefore, these optical bulk parameters can be obtained from first principles, using e.g., Lorenz-Mie theory [van der Hulst 1981; Frisvad

et al 2007]. However, although very successful in practice, this theory neglects the interactions occurring between particles in their near-field, including wave-optics effects such as diffraction and interference with neighbor particles. Consequently, Lorenz-Mie theory is largely limited to isotropic media with relatively low packing rates. Examples of particles arranged as clusters or falling in the near-field region of each other are widespread in nature: From dense media where the particles density and packing rate is large, to spatially-correlated media such as clouds or biological structures where microscopic scatterers form clusters.

Previously, the classical radiative transfer theory has been generalized to handle materials with (statistically) organized microstructures. Anisotropic media [Jakob et al. 2010], for instance, have bulk scattering parameters with stronger directional dependency compared to isotropic media. Additionally, media comprised of particles with correlated locations can exhibit non-exponential transmittance and characteristic scattering profiles [Bitterli et al. 2018; Jarabo et al. 2018]. Although several empirical models have been proposed to model these media, these models work on the macro-scale directly, they are still based on the very same far-field assumption of Lorenz-Mie scattering, and lack the generality to capture wave-optics or multi-spectral effects. Therefore, techniques capable of computing the bulk optical parameters of a material, based on its microscopic properties, have been lacking.

In this paper, we bridge this gap by introducing a new technique to systematically and rigorously compute the bulk scattering parameters. The elementary building block of our technique is particle clusters in which individual particles follow user-specified distributions. Within a cluster, we consider full near-field light transport effects; Between clusters, on the contrary, we use a far-field approximation to allow efficient modeling of macroscopic level light transport.

Our formulation is derived from first principles of light transport (i.e., Maxwell electromagnetism) and reduces to the Lorenz-Mie theory in the special case of single-particle scatterers. Based on this formulation, we demonstrate how the bulk parameters can be computed numerically. Using our technique, we systematically generate radiative transfer optical parameters capturing multi-spectral, anisotropic, and correlated scattering effects for particles with arbitrary distributions (Figure 1).

Concretely, our contributions include:

Establishing a computational framework for modeling light scattering from clusters of particles (Y4).

Showing how radiative transfer parameters can be computed numerically based on our formulation (Y5).

Demonstrating how our technique can be applied to systematically compute scattering parameters for a variety of participating media (Y6).

2 RELATED WORK

Radiative transfer. Simulating the propagation of light in participating media has been widely studied in graphics [Novák et al. 2018], building upon the radiative transfer equation (RTE), introduced 125 years ago by von Lommel [1889] (see [Mishchenko 2013]

for a historical perspective). This scalar radiative formulation has been extended in graphics accounting for anisotropic [Jakob et al. 2010], refractive [Ament et al. 2014], bispectral [Gutierrez et al. 2008], or spatially-correlated media [Jarabo et al. 2018; Bitterli et al. 2018]. All these works assume a radiometric light transport model, establishing no connections with the electromagnetic behaviour governing light transport. From a wave-optics perspective, a few works have generalized light transport in media to account for wave-based properties, including polarized light transport [Wilkie et al. 2001; Jarabo and Arellano 2018], or coherence [Bar. 2019]. This last work is of special relevance, given that it was able to simulate purely wave-based phenomena such as speckle or coherent back-scattering on top of a radiative model. All these works build on the assumption of the far-field approximation and independent scattering, which largely simplifies computations. A notable exception is the near-field model proposed by Bar et al. [2020], that renders speckle statistics in the near-field zone of the camera, although it still considers independent far-field scattering between particles. In contrast, in this work we explicitly relate the radiometric light transport modeled by the RTE with physics-based optics based on electromagnetism, and generalize the independent scattering approximation to account clusters of particles in the near-field.

Modeling scattering in media. The phase function models the average scattering distribution at a light interaction with the medium. A common approach is to use simple phenomenological models, such as the Henyey-Greenstein phase function [Henyey and Greenstein 1941] or mixtures of von Mises-Fisher distributions [Gkioulekas et al. 2013], as well as other functions modeling the scattering of idealized anisotropic particles [Zhao et al. 2011; Heitz et al. 2015]; however, these methods lack an explicit relationship with the underlying microscopic material properties. Under the assumption of geometric optics, several works have proposed to precompute the phase functions of more complex particles for granular materials [Meng et al. 2015; Müller et al. 2016] or cloth fibers [Aliaga et al. 2017] using explicit path tracing, by neglecting wave effects. A more rigorous phase function is based on the Lorenz-Mie theory [van der Hulst 1981], which provides closed-form solutions for the Maxwell's equations for spherical particles [Jackel and Walter 1997; Frisvad et al. 2007]. Sadeghi et al. [2012] generalized the Lorenz-Mie theory to larger non-spherical particles in the context of accurately modeling rainbows. To avoid the expensive sum series of the Lorenz-Mie theory, Guo et al. [2021] proposed to use the geometric optics approximation [Glantschnig and Chen 1981], which gives a good approximation to Lorenz-Mie theory for larger particles at significantly lower cost. All these approaches provide accurate rigorous solutions to the far-field scattering of disperse particles.

Beyond Lorenz-Mie, several exact rigorous solutions have been proposed for computing electromagnetic scattering of particles in media, including the finite elements method (FEM), the finite difference time domain (FDTD) method, or the boundary elements method (BEM) [Wu and Tsai 1977], which solve the Maxwell's equations for arbitrary shapes. Xia et al. [2020] proposed using BEM for accurately precomputing the far-field scattering of individual fibers. Unfortunately these methods are very slow as the number of particles increases, limiting its applicability to individual elements in

problems with reduced dimensionality. The T-matrix method [Walterman 1965] generalizes the Lorentz-Mie theory to particles of arbitrary shape in both the near- and far-fields, with the only assumption of the computed field being outside a sphere surrounding the particles. This method was later extended to clusters of multiple particles [Peterson and Ström 1973; Mackowski and Mishchenko 2011]. We leverage the T-matrix method for computing the scattering of groups of particles.

Wave optics in surface scattering is inspired on the vast background on electromagnetic surface scattering in optics (see [Frisvad et al 2020] for a general survey), several works in graphics have taken into account relevant wave effects including direction-aware BSDFs [He et al 1991; Stam 1999; Cuyper et al 2012; Dong et al 2015; Holzschuch and Pacanowski 2017; Toisoul and Ghosh 2017; Werner et al 2017; Yan et al 2018], goniochromatic patterns due to thin-layer interference [Smits and Meyer 1992; Gondok et al 1994; Belcour and Barla 2017; Guillén et al 2020], or birefringence [Steinberg 2019]. These works assume single scattering, with no interaction between different particles with a few exceptions that assume full incoherence after single scattering [Falster et al 2020; Guillén et al 2020]. Notably, Moravec [1981] and Musbach et al. [2013] computed the full electromagnetic surface scattering by solving the wave propagation using the FDTD method.

3 PRELIMINARIES

We now briefly revisit the basics on first principles of (classical) light transport theory based on Maxwell electromagnetism. Table 1 summarizes the symbols used along the paper.

3.1 Electromagnetic Scattering

The propagation of a time-harmonic monochromatic electromagnetic field with frequency ω is defined by the Maxwell curl equations as

$$\begin{aligned} \text{curl } \mathbf{E}(\mathbf{r}, \omega) &= -i\omega \mathbf{H}(\mathbf{r}, \omega) \\ \text{curl } \mathbf{H}(\mathbf{r}, \omega) &= i\omega \mathbf{Y}(\mathbf{r}, \omega) \mathbf{E}(\mathbf{r}, \omega) \end{aligned} \quad (1)$$

where curl is the curl operator, $\mathbf{E}(\mathbf{r}, \omega)$ and $\mathbf{H}(\mathbf{r}, \omega)$ indicate, respectively, the (vector-valued) electric and magnetic fields at \mathbf{r} and ω , and $\mathbf{Y}(\mathbf{r}, \omega)$ denote the (scalar-valued) magnetic permeability and electric permittivity at \mathbf{r} , respectively; and $i = \sqrt{-1}$ is the imaginary unit.

Assuming a non-magnetic medium satisfying $\mathbf{H}(\mathbf{r}, \omega) = \mathbf{H}_0(\mathbf{r}, \omega)$ with \mathbf{H}_0 being the magnetic permeability of a vacuum, Equation (1) reduces to the electric field wave equation

$$\text{grad}^2 \mathbf{E}(\mathbf{r}, \omega) + \mathbf{Y}(\mathbf{r}, \omega) \mathbf{E}(\mathbf{r}, \omega) = \mathbf{0} \quad (2)$$

where $\text{grad}^2 = \text{div} \text{grad}$, and $\mathbf{Y}(\mathbf{r}, \omega) = \mathbf{Y}(\mathbf{r}, \omega) - \mathbf{Y}_0(\mathbf{r}, \omega)$ is the medium's wave number at \mathbf{r} . Note that the wave number has a dependence on the frequency ω ; in the following we omit such dependence for brevity.

We now assume an infinite homogeneous isotropic medium with permittivity \mathbf{Y}_1 , filled with scatterers bounded by a finite disjoint region \mathcal{V} , with potentially inhomogeneous permittivity \mathbf{Y}_2 . Under this assumption, we can solve Equation (2) by expressing it as the volume integral equation (see §3.1 on the supplemental or §3.1 of Mishchenko's work [2006] for a step-by-step derivation) as the sum of the incident field $\mathbf{E}^{\text{inc}}(\mathbf{r}, \omega)$ and the scattered field $\mathbf{E}^{\text{scat}}(\mathbf{r}, \omega)$ due to

Table 1. Symbols used along the paper.

Symbol	Definition
$\mathbf{r} \in \mathbb{R}^3$	Position
$\hat{\mathbf{s}} \in \mathbb{S}^2$	Direction to \mathbf{r}
$A \in \mathbb{R}$	Distance
$\mathbf{Y}(\mathbf{r}, \omega)$	Permittivity
$\mathbf{H}(\mathbf{r}, \omega)$	Permeability
ω	Wave angular frequency [s^{-1}]
$\lambda = 2\pi/\omega$	Wavelength [m]
$k = \omega/c$	Wavenumber at ω
$n = \sqrt{\mathbf{Y}(\mathbf{r}, \omega)}$	Relative refractive index at ω
$\mathbf{H}^{\text{inc}}(\mathbf{r}, \omega)$	Magnetic field at \mathbf{r}
$\mathbf{E}^{\text{inc}}(\mathbf{r}, \omega)$	Electric field at \mathbf{r} (4)
$\mathbf{E}^{\text{inc}}(\mathbf{r}, \omega)$	Incident electric field
$\mathbf{E}^{\text{scat}}(\mathbf{r}, \omega)$	Scattered electric field at \mathbf{r} (4)
E_0	Amplitude of a planar electric field
$\mathbf{E}^{\text{scat}}(\mathbf{r}, \omega)$	Far-field angular distribution of the scattered radiation
\mathbf{G}_0	Free-space dyadic Green's function (5)
\mathbf{T}	Dyad transition operator (9)
$\mathbf{G}_0^{\text{planar}}$	Planar field scalar propagator
\mathcal{V}	Volume suspended by particle/cluster
$\mathbf{R}_g \in \mathbb{R}^3$	Representative position of particle/cluster
$\hat{\mathbf{s}}_g \in \mathbb{S}^2$	Direction from \mathbf{R}_g to \mathbf{r}
$R_g \in \mathbb{R}$	Distance from \mathbf{R}_g to \mathbf{r}
$\# \text{ cls}$	Number of particles in a cluster
$\mathbf{E}_g^{\text{scat}}(\mathbf{r}, \omega)$	Scattered field of \mathcal{V}_g (8)
$\mathbf{E}_g^{\text{exc}}(\mathbf{r}, \omega)$	Exciting field in \mathcal{V}_g
$\mathbf{E}_g^{\text{exc}}(\mathbf{r}, \omega)$	Partial exciting field in \mathcal{V}_g from particle g (10)
$\mathbf{G}_g^{\text{near}}$	Near-field scattering dyad of particle/cluster (21)
$\mathbf{G}_g^{\text{far}}$	Far-field scattering dyad of particle/cluster (24)
$\sigma_{\text{ext}}^{\text{inc}}(\mathbf{r}, \omega)$	Extinction (29) and scattering (30) cross-sections (1)
$\mathbf{P}(\mathbf{r}, \omega)$	Phase function (31) [s^{-1}]
d	Particles density [m^{-3}]
$f_{\text{ext}}^{\text{inc}}(\mathbf{r}, \omega)$	Extinction (32) and scattering (33) coefficients [m]

inhomogeneities in the medium in the form of scatterers:

$$\begin{aligned} \mathbf{E}(\mathbf{r}, \omega) &= \mathbf{E}^{\text{inc}}(\mathbf{r}, \omega) + \mathbf{E}^{\text{scat}}(\mathbf{r}, \omega) \\ &= \mathbf{E}^{\text{inc}}(\mathbf{r}, \omega) + \int_{\mathcal{V}} \mathbf{Y}(\mathbf{r}', \omega) \mathbf{G}_0(\mathbf{r}, \omega; \mathbf{r}', \omega) \mathbf{E}^{\text{inc}}(\mathbf{r}', \omega) d\mathbf{r}' \end{aligned} \quad (3)$$

with k_1 the wave number at the hosting medium, $n_1 = \sqrt{\mathbf{Y}_1}$ the index of refraction of the interior regions with respect to the hosting medium, the operator \cdot is the dot product and $\mathbf{G}_0(\mathbf{r}, \omega; \mathbf{r}', \omega)$ the free-space dyadic Green's function defined as:

$$\mathbf{G}_0(\mathbf{r}, \omega; \mathbf{r}', \omega) = \mathbf{I} \frac{e^{i k_1 |\mathbf{r} - \mathbf{r}'|}}{4\pi |\mathbf{r} - \mathbf{r}'|} - \frac{\mathbf{r} - \mathbf{r}'}{|\mathbf{r} - \mathbf{r}'|^3} \frac{e^{i k_1 |\mathbf{r} - \mathbf{r}'|}}{4\pi} \quad (5)$$

where \mathbf{I} is the identity dyad, and $\mathbf{a} \mathbf{b}$ denotes the dyadic product of two vectors. Note that the derivative operator ∇ applies over \mathbf{r} . Intuitively, Equation (4) models the scattering field as the superposition of the spherical wavelets resulting from a change of permittivity (i.e. with $n_2 < n_1$). Note also the recursive nature of Equation (4), we will deal with this recursivity in the following section, computing $\mathbf{E}^{\text{scat}}(\mathbf{r}, \omega)$ as a function of the incident field $\mathbf{E}^{\text{inc}}(\mathbf{r}, \omega)$.

¹In the paper we use \cdot as the vector-vector, vector-dyadic and dyadic-dyadic dot products.

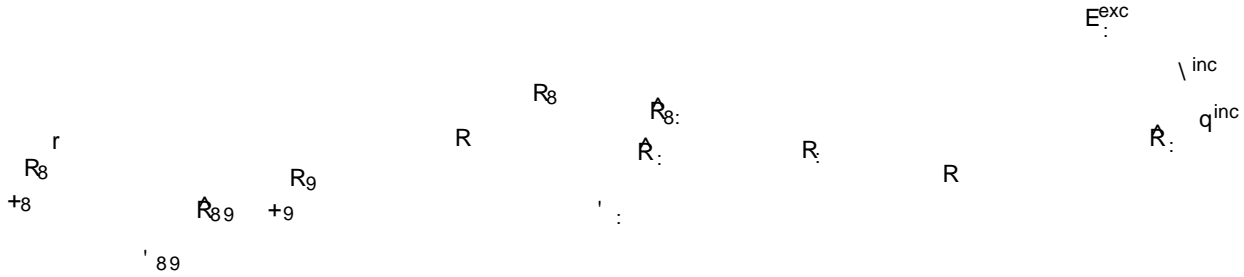


Fig. 2. Schematic representation of the particles scattering geometry. Previous methods, including Lorenz-Mie theory, assume independent scattering of particles (left), assuming that the distance r_{89} between two particles 8 and 9 is very large (i.e., $r_{89} \gg \lambda$), neglecting the potential interactions between particles. In our work (middle) we differentiate between near field scattering of particles within a small region in space (cluster centered at R), and particles 8 and 9 on the far-field region of the cluster (distance $r \gg \lambda$). For large values of r , the direction between particle 8 and any particle 9 is $\hat{R}_8 \approx \hat{R}_9 \approx \hat{R}$. Therefore, we can assume a planar exciting field E^{exc} on the whole cluster from particle 9, with direction \hat{R}_9 (right).

3.2 Foldy-Lax Equations

We now consider a medium filled with finite discrete particles with volume v_8 and index of refraction n_8 . Considering an incident E-field $E^{\text{inc}}(r)$, we can rewrite Equation (4) as

$$E(r) = E^{\text{inc}}(r) + \int_{R^3} \hat{G}(r, r') \cdot \chi(r') E(r') dr' \quad (6)$$

where $\hat{G}(r, r')$ is the dyadic Green's function (5), and $\chi(r')$ the potential function given by

$$\chi(r) = \sum_{s=1}^N \chi_s(r) \quad \text{with} \quad \chi_s(r) = \begin{cases} \chi_s^{\text{ext}}(r) & r \in R_s \\ \chi_s^{\text{int}}(r) & r \in R_s^c \end{cases} \quad (7)$$

By combining Equations (6) and (7), we can express the field at any position $r \in R^3$ following the so-called Foldy-Lax equation [Foldy 1945; Lax 1951] as

$$E(r) = E^{\text{inc}}(r) + \sum_{s=1}^N \int_{R_s} \hat{G}(r, r') \cdot \chi_s(r') E(r') dr' \quad (8)$$

with $E_s^{\text{scat}}(r)$ and $E_s^{\text{part}}(r)$ the scattered and partial field of particle 8 and $\hat{G}_s(r, r')$ the dyadic transition operator for particle 8 defined as [Tsang et al. 1985]

$$\hat{G}_s(r, r') = \chi_s(r) X_1(r - r') \quad (9)$$

with $X_1(r)$ the Dirac delta. The partial field at particle 8 is defined as $E_8^{\text{part}}(r) = E^{\text{inc}}(r) + \sum_{g \neq 8} E_{8g}^{\text{exc}}(r)$, where the partial exciting field $E_{8g}^{\text{exc}}(r)$ from particles 9 to 8 is

$$E_{8g}^{\text{exc}}(r) = \int_{R_g} \hat{G}_8(r, r') \cdot \chi_g(r') E(r') dr' \quad (10)$$

with $r \in R_8$. Note that the scattered and exciting fields for particle 9 have essentially the same form. As shown by Mishchenko [2002], the Foldy-Lax equation (8) solves exactly the volume integral equation (4) for multiple arbitrary particles in the medium, without

any assumptions on their composition or packing rate, beyond the assumption of a homogeneous hosting medium.

Far-field Foldy-Lax Equation (10) defines the exact exciting field resulting from the scattering by particle 9 on particle 8. However, if the distance $r_{89} = |R_8 - R_9|$ between particles (with R_8 denoting the center of particle 8) is large, we can approximate the propagation distance between any point $r \in R_8$ and $r' \in R_9$ as

$$|r - r'| \approx r_{89} + \hat{R}_{89} \cdot (r - r') \quad (11)$$

with $\hat{R}_{89} = (R_8 - R_9)/r_{89}$, $r := r - R_8$ and $r' := r' - R_9$ (see Figure 2, left). With this approximation, we can now express $E_{8g}^{\text{exc}}(r)$ for a point $r \in R_8$ using its far-field approximation (see Appendix 3 in the supplemental for the derivation), as

$$E_{8g}^{\text{exc}}(r) = \frac{\exp(i k r_{89})}{r_{89}} \hat{R}_{89} \cdot E_{18g}^{\text{exc}}(r) \quad (12)$$

with $r \in R_8$ a point in particle 8 $E_{18g}^{\text{exc}}(r) = \exp(i k r_{89}) \hat{R}_{89} \cdot E_{18g}^{\text{exc}}(r)$ the far-field exciting field from particle 9 to particle 8 defined as

$$E_{18g}^{\text{exc}}(r) = \int_{R_g} \hat{G}_8(r, r') \cdot \chi_g(r') E(r') dr' \quad (13)$$

The dyadic $\hat{R}_{89} \hat{R}_{89}$ ensures a transverse planar field, which allows to solely characterize $E_{18g}^{\text{exc}}(r)$ by the propagation direction \hat{R}_{89} . In order for Equation (12) to be valid, the distance r_{89} needs to hold the far-field criteria, which relates the distance r_{89} with the radius of the particle a_9 following the inequality [Mishchenko et al. 2006]:

$$r_{89} \gg \max\left\{ \frac{2a_9^2}{\lambda}, a_9 \right\} \quad (14)$$

This far-field assumption is both the basis for the Lorenz-Mie theory [van der Hulst 1981] (to model electromagnetic scattering from small spherical particles) and, as shown by Mishchenko [2002], at the core of the radiative transfer theory.

In the following, we relax the assumption of near-field scattering and compute the Foldy-Lax equations for clusters of particles for both the near- and far-field regions. Then, we use them to compute

the scattering matrix to be used in the RTE to efficiently approximate light transport between clusters of particles.

4 SCATTERING FROM CLUSTERS OF PARTICLES

In this section, we present our main theoretical result: the far-field approximated scattering dyad relating a field incoming at a particle, which will be shown in Equation (24). This dyad can then be used to compute a medium's bulk scattering parameters, which we will discuss in §4.1.

The two forms of computing the exciting field from particles to \mathbf{r}^0 [Equations (10) and (12)] suggest that we can consider two subsets of particles depending on their distance with respect to the point of interest: One set of $\#_{\text{near}}$ particles in the near field and another set of $\#_{\text{far}}$ particles in the far field. With that, we can now calculate the exciting field in particle \mathbf{r}^0 as

$$\mathbf{E}_{\mathbf{r}^0}^{\text{exc}} = \mathbf{E}^{\text{inc}}(\mathbf{r}^0) + \sum_{g' < g = 1}^{\#_{\text{near}}} \mathbf{E}_{\mathbf{r}^0}^{\text{exc}} + \sum_{g' = 1}^{\#_{\text{far}}} \mathbf{E}_{\mathbf{r}^0}^{\text{exc}} \quad (15)$$

In what follows, we derive the far-field Foldy-Lax equations for groups of particles where a cluster of these particles are in their respective near-field region, while the other elements in the system are in the far field. For the simplicity of our derivations, we consider a single far-field incident field in the cluster, and assume that the far-field particles do not have neighbor particles in their respective near-field region. More formally, we now consider a cluster of $\#$ particles, where all particles \mathbf{r}^0 are in their respective near-field region, and that the particles of the cluster have a bounding sphere centered at \mathbf{R} with radius R (see Figure 2, middle).

Since both the incident field $\mathbf{E}^{\text{inc}}(\mathbf{r}^0)$ and the exciting field $\mathbf{E}_{\mathbf{r}^0}^{\text{exc}}$ from particle \mathbf{r}^0 are in the far-field region, we can assume both fields to be planar waves defined as

$$\mathbf{E}^{\text{inc}}(\mathbf{r}^0) = \mathbf{E}_0^{\text{inc}} \exp(i \mathbf{k}^{\text{inc}} \cdot \mathbf{r}^0) = \mathbf{E}_0^{\text{inc}} \mathbf{G}^{\text{inc}}(\mathbf{r}^0) \quad (16)$$

$$\mathbf{E}_{\mathbf{r}^0}^{\text{exc}} = \mathbf{E}_0^{\text{exc}} \exp(i \mathbf{k}^{\text{exc}} \cdot \mathbf{r}^0) = \mathbf{E}_0^{\text{exc}} \mathbf{G}^{\text{exc}}(\mathbf{r}^0) \quad (17)$$

with $\mathbf{E}_0^{\text{inc}}$ the amplitude of the planar incident field in its direction, and $\mathbf{r} = \mathbf{r}^0 - \mathbf{R}$. Equivalently, $\mathbf{E}_0^{\text{exc}} = \frac{\exp(i \mathbf{k}^{\text{exc}} \cdot \mathbf{R})}{\mathbf{G}^{\text{exc}}(\mathbf{R})} \mathbf{E}_1^{\text{exc}}(\mathbf{R})$ is the amplitude of the exciting field at \mathbf{r}^0 from particle \mathbf{r}^0 , and \mathbf{R} is its direction.

Now, let us slightly abuse the dot product notation, remove the dependency on the spatial dependency on each term, and use $i_2^0 = i_1^1 \mathcal{G}^i i_2^1 \mathcal{G}^d \mathbf{G}$ for scalar-valued functions i_1 and i_2 . From the far-field assumptions, plugging Equation (15) into the definition of the scattered field from particle \mathbf{r}^0 in Equation (8) (with $\#_{\text{near}} = \#^{\text{cls}}$) yields

$$\mathbf{E}_{\mathbf{r}^0}^{\text{sca}} = \mathbf{E}_0^{\text{inc}} \mathbf{G}^{\text{inc}}(\mathbf{r}^0) + \sum_{g' < g = 1}^{\#_{\text{near}}} \mathbf{E}_{\mathbf{r}^0}^{\text{exc}} + \sum_{g' = 1}^{\#_{\text{far}}} \mathbf{E}_{\mathbf{r}^0}^{\text{exc}} \quad (18)$$

By recursively expanding $\mathbf{E}_{\mathbf{r}^0}^{\text{exc}}$ and some algebraic operations (see the supplemental for the full derivation), this results into

$$\mathbf{E}_{\mathbf{r}^0}^{\text{sca}} = \mathbf{E}_0^{\text{inc}} \mathbf{G}^{\text{inc}}(\mathbf{r}^0) + \sum_{g' < g = 1}^{\#_{\text{near}}} \mathbf{E}_{\mathbf{r}^0}^{\text{exc}} + \sum_{g' = 1}^{\#_{\text{far}}} \mathbf{E}_{\mathbf{r}^0}^{\text{exc}} \quad (19)$$

where the domain of integration in the spatial domain of \mathbf{r}^0 is $\mathbf{r}^0 = \mathbf{r}^0 - \mathbf{R}$, and $\mathbf{G}^{\text{inc}}(\mathbf{r}^0)$ term represents the recursivity as

$$\mathbf{G}^{\text{inc}}(\mathbf{r}^0) = \mathbf{G}^{\text{inc}}(\mathbf{r}^0) + \sum_{g' < g = 1}^{\#_{\text{near}}} \mathbf{G}^{\text{inc}}(\mathbf{r}^0) \quad (20)$$

Note this recursivity is similar to the one appearing in the rendering equation [Kajiya 1986]. Each element in the sum in Equation (19) above is the result of the amplitude of the far-field incident or exciting fields, and a series that encode all the near-field scattering in the cluster. We can thus define the scattering dyad $\mathbf{E}_{\mathbf{r}^0}^{\text{sca}}(\mathbf{r}^0)$ relating a unit-amplitude planar incident field at particle \mathbf{r}^0 from direction \mathbf{n}^{inc} with the scattered field at point \mathbf{r}^0 as

$$\mathbf{E}_{\mathbf{r}^0}^{\text{sca}}(\mathbf{n}^{\text{inc}}) = \mathbf{E}_0^{\text{inc}} \mathbf{G}^{\text{inc}}(\mathbf{r}^0) + \sum_{g' < g = 1}^{\#_{\text{near}}} \mathbf{E}_{\mathbf{r}^0}^{\text{exc}}(\mathbf{n}^{\text{inc}}) \quad (21)$$

By considering constant $\mathbf{E}_0^{\text{inc}}$ and $\mathbf{E}_0^{\text{exc}}$ for the whole cluster, we can compute the cluster's scattering dyad as

$$\mathbf{E}_{\mathbf{r}^0}^{\text{sca}}(\mathbf{n}^{\text{inc}}) = \mathbf{E}_0^{\text{inc}} \mathbf{G}^{\text{inc}}(\mathbf{r}^0) + \sum_{g' < g = 1}^{\#_{\text{near}}} \mathbf{E}_{\mathbf{r}^0}^{\text{exc}}(\mathbf{n}^{\text{inc}}) \quad (22)$$

which defines the scattered field for a unit-amplitude incoming planar field in a scene consisting of the particles forming cluster. In practice, the scattering dyad $\mathbf{E}_{\mathbf{r}^0}^{\text{sca}}(\mathbf{n}^{\text{inc}})$ can be computed numerically using standard methods from computational electromagnetics (see §5 for more details).

Far-field approximation Equation (21) represents the general form of the scattering dyad for particle \mathbf{r}^0 which results into a vector-dimensional function. Assuming that is in the far-field region of a particle \mathbf{r}^0 , by using the far-field approximation of the scattered or exciting field (12) (we refer to the supplemental document for the derivation), we get the scattered field by particle \mathbf{r}^0 as

$$\mathbf{E}_{\mathbf{r}^0}^{\text{sca}} = \frac{4\pi \mathbf{r}^0}{3} \mathbf{G}^{\text{inc}}(\mathbf{r}^0) + \sum_{g' < g = 1}^{\#_{\text{near}}} \mathbf{E}_{\mathbf{r}^0}^{\text{exc}}(\mathbf{n}^{\text{inc}}) \quad (23)$$

with $\mathbf{r}^0 := \mathbf{r}^0 - \mathbf{R}$ and $\mathbf{R} := \mathbf{r}^0 - \mathbf{r}^0$, and

$$\mathbf{G}^{\text{inc}}(\mathbf{r}^0) = \mathbf{G}^{\text{inc}}(\mathbf{r}^0) + \sum_{g' < g = 1}^{\#_{\text{near}}} \mathbf{G}^{\text{inc}}(\mathbf{r}^0) \quad (24)$$

300nm 600nm 900nm

Fig. 3. Comparison against Lorenz-Mie theory: We compare our method with clusters containing a single particle (i.e., $\#_{cls} = 1$) against a reference solution based on Lorenz-Mie theory for three different particle radii 0.2 f 300nm, 600nm, 900nm. As expected, for a single particle our method reduces to the same results as Lorenz-Mie theory. The wavelength is $\lambda = 600$ nm, while the refractive index of the particle is $n = 1.5$, $0.1i$.

Finally, since $\hat{\mathbf{R}}_g = \hat{\mathbf{R}}$ for all particles $g \in \mathcal{G}$, we can approximate the far-field scattered field of cluster as

$$\mathbf{E}^{sca, \mathbf{r}^0} = \frac{4\pi}{r^2} \sum_{g=1}^{\#_{cls}} \hat{\mathbf{R}}_g \cdot \mathbf{E}_0, \quad \hat{\mathbf{R}}_g = \hat{\mathbf{R}} \cdot \mathbf{e}_g \cdot \mathbf{E}_0^{exc} \cdot (25)$$

where

$$\hat{\mathbf{R}}_g \cdot \mathbf{E}_0^{exc} = \sum_{g=1}^{\#_{cls}} \hat{\mathbf{R}}_g \cdot \mathbf{E}_0^{exc} \cdot (26)$$

is the far-field scattering dyad of cluster.

Thus, by grouping the individual particles into $\#_{cls}$ near-field clusters, and assuming that all clusters and observation point lay in their respective far-field, we can approximate the Foldy-Lax equation (8) as

$$\mathbf{E}^{\mathbf{r}^0} = \mathbf{E}^{inc, \mathbf{r}^0} + \sum_{g=1}^{\#_{cls}} \mathbf{E}^{sca, \mathbf{r}^0} \cdot (27)$$

with $\mathbf{E}^{sca, \mathbf{r}^0}$ the scattered field at cluster g .

4.1 Relationship with the Radiative Transfer Theory

The scattering dyad $\hat{\mathbf{R}}_g \cdot \mathbf{E}_0^{exc}$ given by Equation (26) models how a particles cluster scatters a planar unit-amplitude incident field from direction $\hat{\mathbf{n}}^{inc}$ towards direction $\hat{\mathbf{n}}^{sca}$ in the far-field region. However, for rendering we are generally interested on the average field intensity (i.e., radiance).

As shown by Mishchenko [2002], the radiative transfer equation (RTE) directly derives from the far-field Foldy-Lax equations under three additional assumptions: (i) The amount of coherent backscattering is negligible; (ii) The particles are randomly distributed according to some distribution $\mathcal{P}(\mathbf{r}^0, \mathbf{b}_g)$, with \mathbf{r}^0 and \mathbf{b}_g denoting, respectively, the position and properties (e.g., shape, size, index of refraction...) of a particle g and (iii) We are interested on the average field $\langle \mathbf{E}^{\mathbf{r}^0} \rangle$.

Following these assumptions, and after a lengthy derivation, Mishchenko demonstrates that the bulk scattering properties can be obtained from the far-field Foldy-Lax form, and in particular from the scattering dyad $\hat{\mathbf{R}}_g \cdot \mathbf{E}_0^{exc}$. Let us first assume that the distribution of particle properties \mathcal{P} are independent of the particles

position, and compute the average scattering dyad $\langle \hat{\mathbf{R}}_g \cdot \mathbf{E}_0^{exc} \rangle = \int \hat{\mathbf{R}}_g \cdot \mathbf{E}_0^{exc} \cdot \mathcal{P}(\mathbf{r}^0, \mathbf{b}_g) d\mathbf{r}^0 d\mathbf{b}_g$. Then, note that the Foldy-Lax equation for clusters of particles (27) we derived above has the same form as the original Foldy-Lax equation (8). Thus, by the same derivation followed by Mishchenko we get to an equivalent RTE based on the scattering dyad of clusters.

Computing the scattering parameters by taking the vectors of the parallel and perpendicular polarization $\hat{\mathbf{s}}^{inc}$ and $\hat{\mathbf{s}}^{sca}$ of the incident field as shown in Figure 2 (right), and equivalently for the scattered field $\hat{\mathbf{s}}^{sca}$ and $\hat{\mathbf{s}}^{inc}$, we can compute the polarized scattering components χ and γ_q from the average cluster's scattering dyad $\hat{\mathbf{R}}_g \cdot \mathbf{E}_0^{exc}$ as

$$\begin{aligned} \chi &= \langle \hat{\mathbf{s}}^{sca} \cdot \hat{\mathbf{R}}_g \cdot \hat{\mathbf{s}}^{inc} \rangle = \langle \hat{\mathbf{s}}^{sca} \cdot \hat{\mathbf{R}}_g \cdot \hat{\mathbf{s}}^{inc} \rangle \\ \gamma_q &= \langle \hat{\mathbf{s}}^{sca} \cdot \hat{\mathbf{R}}_g \cdot \hat{\mathbf{s}}^{inc} \rangle = \langle \hat{\mathbf{s}}^{sca} \cdot \hat{\mathbf{R}}_g \cdot \hat{\mathbf{s}}^{inc} \rangle \end{aligned} \quad (28)$$

Then, based on the two scattering components χ and γ_q , we can obtain the optical parameters of the medium as

$$\Lambda_t^{inc} = 4c \langle \chi \rangle \cdot (29)$$

$$\Lambda_s^{inc} = \frac{j \langle \chi \rangle^2 + j \langle \gamma_q \rangle^2}{2 \langle \chi \rangle^2} d \hat{\mathbf{n}}^{sca} \cdot (30)$$

$$\Lambda_p^{inc} = \frac{j \langle \chi \rangle^2 + j \langle \gamma_q \rangle^2}{2 \langle \chi \rangle^2} d \hat{\mathbf{n}}^{sca} \cdot (31)$$

with $\langle \chi \rangle = \langle \chi \rangle$, $\langle \gamma_q \rangle = \langle \gamma_q \rangle$, $\langle \chi \rangle = \langle \chi \rangle$, $\langle \gamma_q \rangle = \langle \gamma_q \rangle$ returning the real part of a complex number $\langle \chi \rangle$ and S^2 the unit sphere of directions. Lastly, assuming a uniform distribution of clusters, we can compute the extinction and scattering coefficients as

$$f_t^{inc} = \Lambda_t^{inc} \frac{d}{\#_{cls} \cdot (32)$$

$$f_s^{inc} = \Lambda_s^{inc} \frac{d}{\#_{cls} \cdot (33)$$

with d the number of particles per differential volume, and $\#_{cls}$ the average number of particles per cluster. Note that the optical properties defined in Equations (29) (33) are directionally dependent, so they are general and can represent both isotropic and anisotropic media.

4.2 Relationship with Independent Scattering

Most previous works rendering light transport in media [Novák et al. 2018] build on the assumption of independent scattering that is, particles are in their respective far-field region. It is easy to verify that this is a special case of Equation (15) with $\#_{cls} = 1$, causing the scattering dyad of Equation (26) to reduce to

$$\hat{\mathbf{R}}_g \cdot \mathbf{E}_0^{exc} = \hat{\mathbf{R}}_g \cdot \mathbf{E}_0^{exc} = \frac{6 \hat{\mathbf{n}}^{sca} \cdot \hat{\mathbf{R}}_g \cdot 6 \hat{\mathbf{n}}^{inc}}{4c} \cdot (34)$$

which encodes the scattered field in the far-field region of a particle when excited by an incident unit-amplitude planar field. The Lorenz-Mie theory [van der Hulst 1981] provides closed-form expressions

Fig. 4. Comparison against Lorenz-Mie theory: We compare the extinction and scattering cross sections computed with our method for $\# \text{cls} = 1$ against the results obtained using Lorenz-Mie theory. As in Figure 3, our results show perfect agreement.

for $\int_{\Omega} \mathbf{n}^{\text{inc}} \cdot \mathbf{n}^{\text{sca}} d\Omega$ for spheres and cylinders, while numerical solutions of $\int_{\Omega} \mathbf{n}^{\text{inc}} \cdot \mathbf{n}^{\text{sca}} d\Omega$ have been proposed for scatterers of arbitrary shapes via, for example, the T-matrix method [Waterman 1965], or more recently based on the BEM for cylindrical bodies [Xia et al 2020]. Our work is therefore a generalization of these works to particles in the near field.

5 COMPUTING THE BULK SCATTERING PARAMETERS

We now detail our numerical computations of the scattering dyad $\int_{\Omega} \mathbf{n}^{\text{inc}} \cdot \mathbf{n}^{\text{sca}} d\Omega$ of Equation (26) which in turn determines the bulk scattering parameters following Equation (33). These bulk scattering parameters can be directly used in any renderer supporting participating media [Novák et al 2018] using tabulated phase function and cross sections.

Computing $\int_{\Omega} \mathbf{n}^{\text{inc}} \cdot \mathbf{n}^{\text{sca}} d\Omega$ essentially boils down to solving the time-harmonic Maxwell equations for an incident unit-amplitude planar field with direction \mathbf{n}^{inc} . While several different methods exist for that purpose (see §16 of [Mishchenko 2014] for an overview), we opt for the superposition T-matrix method [Mackowski and Mishchenko 1996] that has been demonstrated efficient for moderately large $\# \text{cls}$, can handle scatterers with arbitrary geometry, and is based on the principles of the Foldy-Lax equations, making it particularly appealing for our work.

In practice, we use the open-source CUDA-based LESolver [Egel et al 2017], which implements the superposition T-matrix method proposed by Mackowski and Mishchenko [2011] for spherical or randomly rotated particles. In our implementation, we focus on clusters of spherical particles. Since the Lorenz-Mie theory also assumes spherical particles, this allows us to directly compare our results with those computed using the Lorenz-Mie theory (see Figures 3 and 4). Note that the T-matrix method does not introduce assumptions on the size of particles but, similar to Lorenz-Mie theory, larger particles result in more expensive computations.

To compute the average scattering dyad $\int_{\Omega} \mathbf{n}^{\text{inc}} \cdot \mathbf{n}^{\text{sca}} d\Omega$, we average the scattered field of several random realizations of the clusters (each of which obtained by randomly sampling the position of the particles inside the cluster's bounding sphere). As

we will demonstrate in §6, we use a wide array of distributions including particles uniformly distributed over the volume of the cluster, positively-correlated particles following Shaw et al. [2002], negatively-correlated particles using Poisson sampling of the sphere, and anisotropic distributions by uniformly sampling the particles on a oriented 2D disk.

Lastly, we represent the resulting phase function as well as the extinction and scattering cross sections as tabulated (i.e., piecewise constant) functions that can be used for rendering.

6 EXPERIMENTS

In this section, we first validate our technique by comparing bulk scattering parameters computed with our method and the Lorenz-Mie theory (§6.1). Then, we apply our technique described in §4 and §5 to compute bulk scattering parameters for a wide range of participating media (§6.2).

6.1 Validation

To validate our technique, we compare computed bulk scattering parameters provided by our implementation and MiePlot [Laven 2011], a free software based on the Lorenz-Mie theory. We focus on the configuration where a cluster contains only one (spherical) particle as this is a fundamental assumption of the Lorenz-Mie theory.

In Figure 3, we visualize computed single-scattering phase functions at the wavelength 600 nm with three particle radii (300, 600, and 900 nm). We set the refractive index of the particle to 1.5. Additionally, we show in Figure 4 the corresponding extinction and scattering cross sections σ_{ext} and σ_{sca} given by Equation (29) and (30) respectively. In all these examples, our computed scattering parameters match those predicted by the Lorenz-Mie theory perfectly.

6.2 Main Results

We now demonstrate the versatility of our technique by computing bulk scattering parameters for a range of participating media. In all cases, we set the cluster size to roughly the same order of magnitude of the coherence area of sunlight. This allows us to assume an incident planar field. Further, we assume that particles outside the cluster might receive different incident field. Then, light scattering outside the cluster is assumed to be sufficiently far away, following the central assumption of RTT.

By default, we set the refractive indices of the particles and the embedding media to 1.5 and 1, respectively. Please see Table 2 for the performance statistics of our experiments.

Isotropic media In computer graphics, volumetric light transport effects are typically simulated using isotropic media where the extinction and scattering coefficients f_t, f_s are directionally independent, and the single-scattering phase function p is formulated as a 1D function on the angle between the incident and scattered directions.

Our technique can produce bulk scattering parameters for isotropic media using particles distributed in radially symmetric densities. We conduct a few ablation studies to demonstrate how different particle arrangements in a cluster affect the resulting parameters. We use a wavelength of 700 nm for all these studies and represent the

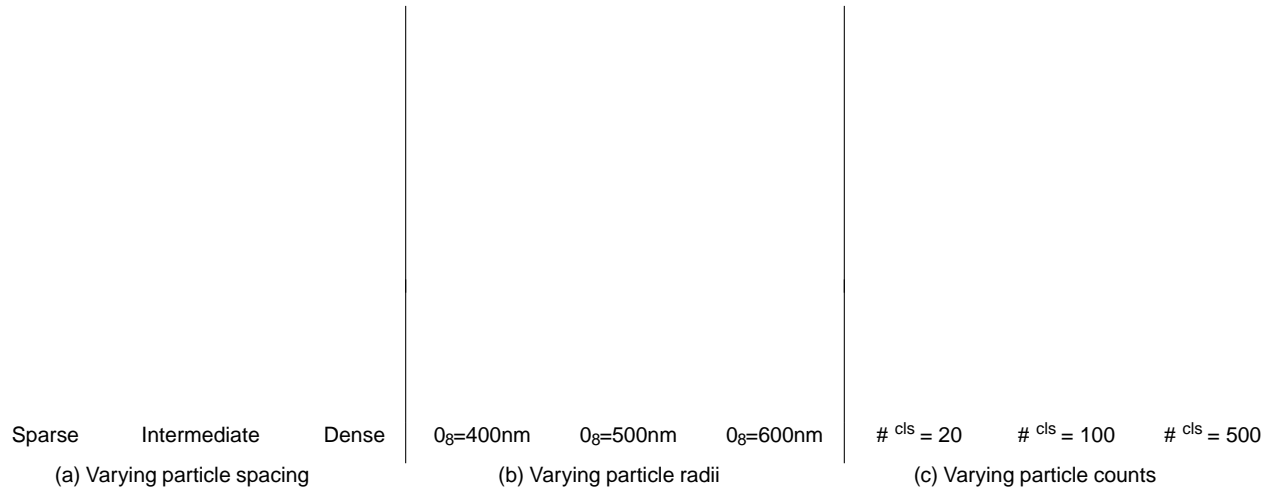


Fig. 5. Comparison of the resulting (normalized) phase function for different cluster parameters, for a planar incident field at $\lambda = 700$ nm. Unless mentioned otherwise, the clusters have $\# \text{ cls} = 100$ particles, and each particle has radius $r_g = 500$ nm. For each phase function, we vary: (a) The distance between particles within the cluster; (b) The particle size r_g ; and (c) The number of particles $\# \text{ cls}$. We visualize all phase functions in logarithmic scale to better show their low-magnitude regions.

1D phase functions as tabulated (i.e., piecewise constant) functions using 180 equal-sized bins.

In our first study, we use a cluster of 100 particles with radii 500 nm. Then, we vary the distances between particles (by using bounding spheres with different sizes and distributing particles uniformly in these spheres). As shown in Figure 5 (a), the closer the particles are to each other, the more forward the resulting phase function is. This is expected: With sparsely distributed particles, it is simpler for light to pass straightly through.

Our second ablation study examines the effect of particle size. With 100 uniformly distributed particles, we apply our technique to three particle sizes $r_g = 400, 500,$ and 600 nm. As shown in Figure 5 (b), as we increase the particles radius, the phase function becomes more forward and increases its frequency. This agrees with the behaviour of single particles predicted by Lorenz-Mie theory.

In our third study, we vary the number of particles in a cluster while keeping the particle size fixed to $r_g = 500$ nm. Figure 5 (c) shows that as we increase the number of particles, the phase function gets more forward and of higher-frequency, in a behaviour somewhat correlated with the particles size. This is the result of the increasing number of diffractive elements on the cluster, that instead of making scattering more diffuse (as predicted by geometric optics) increases its forward frequency.

Lastly, we show in Figure 6 monochrome renderings using bulk scattering parameters obtained with varying combinations of particle count and radius.

Multi-spectral results Since our technique is derived using microphysical wave optics, it allows systematic generation of multi-spectral parameters based on a single (monochrome) configuration of particle cluster.

To demonstrate this, we use a configuration of 100 uniformly distributed particles (per cluster) with radius 500 nm and compute

bulk scattering parameters at 50 wavelengths ranging from 400 nm to 700 nm. In Figure 7, we visualize the computed phase functions at five wavelengths as well as multi-spectral renderings of a backlit thin slab. The smooth changes in scattering parameters across wavelength have resulted in a characteristic rainbow-like effect. When using the single-particle configuration (with identical overall particle density per unit volume), the rainbow effect is missing.

Figure 8 shows renderings of the Lucy model using these scattering parameters.

Varying particle refractive index We show in Figure 9 how the refractive index of the particles affects the final appearance. In this example, all four media is formed by clusters of 100 particles with radii 500 nm. We keep the imaginary part of refractive index k and vary the real part from 1.2 to 1.5 . Increasing the refractive index leads to a stronger backward scattering, which makes the rendered object less transparent.

Varying particle sizes Our technique supports clusters comprised of particles with varying sizes. In Figure 10, we illustrate how variations of particle sizes affects macro-scale object appearance. Specifically, on the top of this figure, we show bulk phase functions of four isotropic media generated using our method with $\# \text{ cls} = 100$ and uniformly distributed particles. Further, the particle sizes per cluster follow normal distributions with the mean 300 nm and standard deviations varying from 20 nm to 200 nm.

The bottom of Figure 10 shows renderings of the Lucy model using the four media. We can see that, when the variation in particle sizes increases, the object tends to appear overall more opaque (i.e., with lower light transmission).

Anisotropic media Anisotropic media allow the extinction and scattering coefficients t, f_s to be directionally dependent, and have

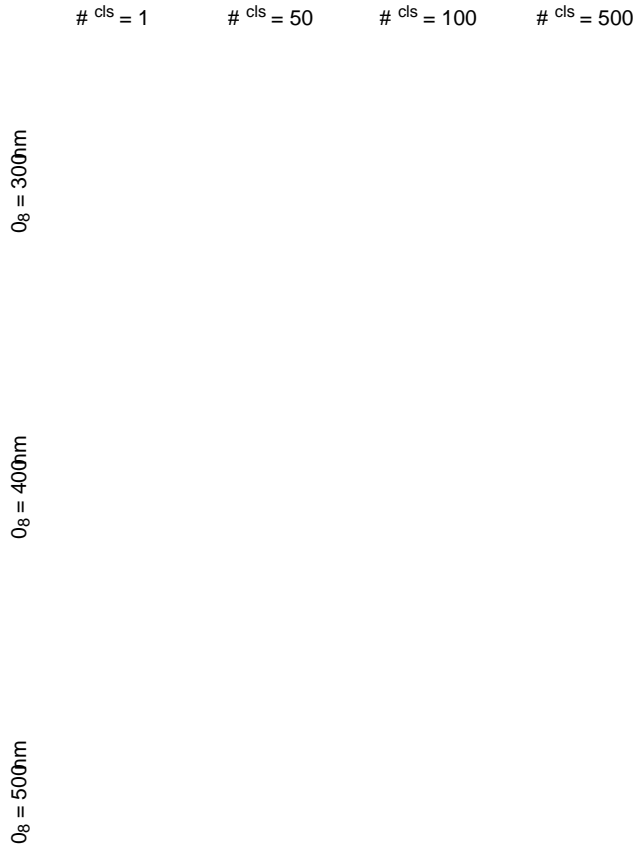


Fig. 6. Renderings of homogeneous Lucy models at 700nm. The bulk scattering parameters are computed using our method with different combinations of particle radius r_g and per-cluster particle count n_{cls} .

full 4D phase functions Φ_p . Previously, although the scattering parameters of anisotropic media can be devised based on the microscopic models [Jakob et al2010; Heitz et al2015], equivalences of the Lorenz-Mie theory, to our knowledge, have been lacking.

By using anisotropic particle distributions, our technique can generate bulk scattering parameters for anisotropic media. To demonstrate this, we use a configuration where the cluster contains $n_{cls} = 100$ particles following an anisotropic Gaussian distribution, as illustrated in Figure 11 (a). We tabulate the extinction and scattering cross sections using the latitude-longitude parameterization with a resolution of 180×360 . Due to the symmetry of the disc, the resulting phase function Φ_p is three-dimensional, and we tabulated it with the resolution $90 \times 180 \times 360$.

In Figure 11 (b), we visualize slices of the computed single-scattering phase function Φ_p with two incident directions \mathbf{n}^{inc} . In Figure 12, we show renderings of the Lucy model with three (spatially invariant) orientations.

Ours

Single-particle

(a) Phase function

(b) Thin-slab rendering

Fig. 7. Multi-spectral results: (a) visualizations of phase functions; (b) corresponding multi-spectral renderings of a thin slab lit by a small area light from behind. Results on the top are generated using a cluster of 100 particles with radii 500nm. Results on the bottom are obtained using a conventional single-particle setting. We used identical particle counts per differential volume for both configurations.

(a) Multi. (b) 400nm (c) 550nm (d) 700nm

Fig. 8. (a) Multi-spectral rendering of a homogeneous Lucy model using identical bulk scattering parameters as the top row of Figure 7. (b-d) Monochrome renderings of the same model at three wavelengths.

Correlated particles. In Figure 13, we demonstrate the effect of particles correlation within the cluster, by analyzing particles distributed using both negative (Poisson sampled) and positive correlation [Jarabo et al2018]. We compare the effect of introducing microscopic correlation on media where the clusters position is itself correlated, compared with uniformly distributed particles inside the clusters. These two levels of correlation have significant effect on the final appearance of the translucent materials.

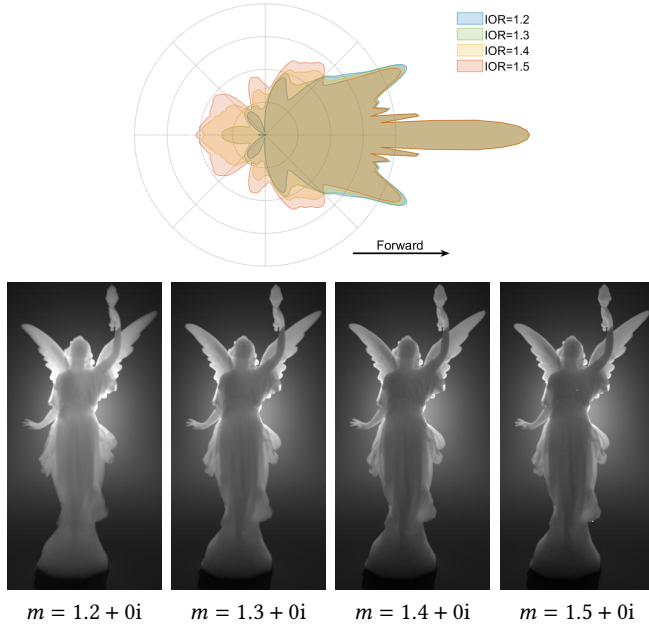


Fig. 9. Effect of the refractive index of the particles. The top of this figure visualizes the bulk phase functions of clusters of 100 particles with radii 500nm. The refractive index of the particles range from $m = 1.2 + 0i$ to $1.5 + 0i$ suspended in the vacuum. The bottom figures show renderings of the Lucy model for media with each refractive index.

Table 2. Performance statistics for our simulation. The numbers are collected using a workstation equipped with an Intel i7-6800K six-core CPU and an Nvidia GTX 1080 GPU. Timings are given for each random realization of the particles within the cluster; to compute the average scattering dyad we average 50 realizations.

	N^{cls}	f_p res.	time
Regular (Fig. 6)	1–500	180×360	3–16s
Multi-spectral (Fig. 8)	100	$180 \times 360 \times 50$	35m
Varying particle sizes (Fig. 10)	100	180×360	7–108s
Anisotropic (Fig. 12)	100	$180 \times 360 \times 90$	13m
Correlated (Fig. 13)	100	180×360	98s

7 DISCUSSION AND CONCLUSION

Limitations and future work. While taking into account the effect of the near-field on clusters, our work is still based on the RTT. Therefore it relies on the far-field approximation to represent a scattering dyad useful for rendering. Therefore, while we can handle near- and far-field scattering, we cannot accurately model the scattering in the intermediate region, which we treat as the far field. Using more accurate representations, that capture the effects at such mid-field region could further enhance the generality of our theory and, thus, is an interesting future topic. This would however require exploring an alternative light transport framework beyond the RTT. Recent light transport models tracking light coherence [Steinberg

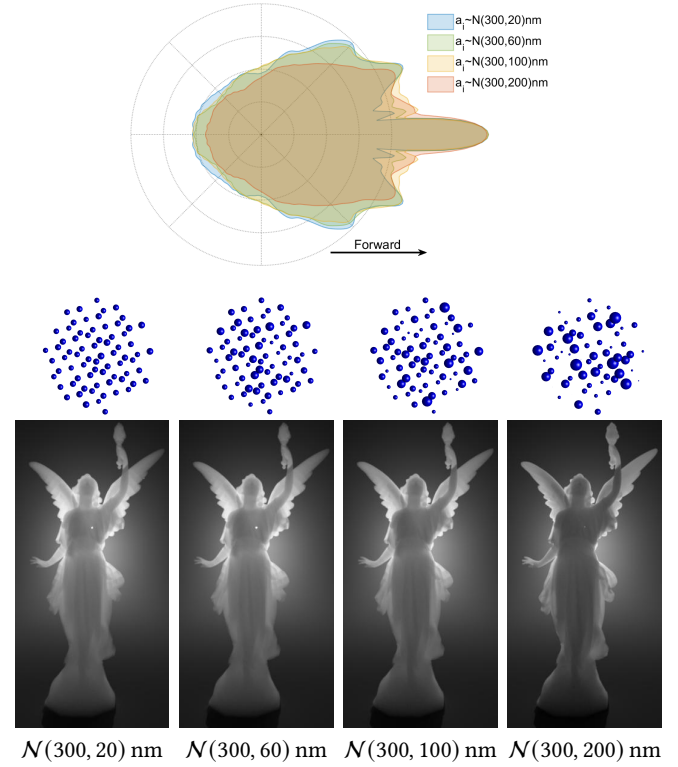


Fig. 10. Our technique supports clusters comprised of particles with varying sizes. The top of this figure visualizes bulk phase functions of four media generated with $N^{\text{cls}} = 100$ and uniformly distributed particles. Further, sizes of particles in each cluster are normally distributed with the same mean (300nm) but varying standard deviations (20nm, 60nm, 100nm, and 200nm). The bottom of this figure shows renderings of the Lucy model made of the four media, respectively.

and Yan 2021] are a promising framework for modeling such mid-field scattering.

Our current implementation requires precomputing the bulk optical properties of the media. This limits the applicability of our work to media with homogeneous particle statistical properties. Finding faster approximations for our scattering functions, in the same spirit as the geometric optics approximation for Lorenz-Mie theory [Glantschnig and Chen 1981], is an interesting future research. An efficient analytic approximation would also be very useful for fitting real-world measurements as well as in inverse scattering applications, which are now limited by the expensive precomputation.

Finally, while our theory is fully general in terms of particles shape, composition, and distribution, our implementation is currently limited in practice to clusters of spherical particles. Allowing arbitrary particle shapes by using an alternative implementation of the T-matrix method would further improve the versatility of our technique.

Conclusion. In this paper, we introduce a new technique to systematically compute bulk scattering parameters for participating media. Built upon first principles of light transport (i.e., Maxwell

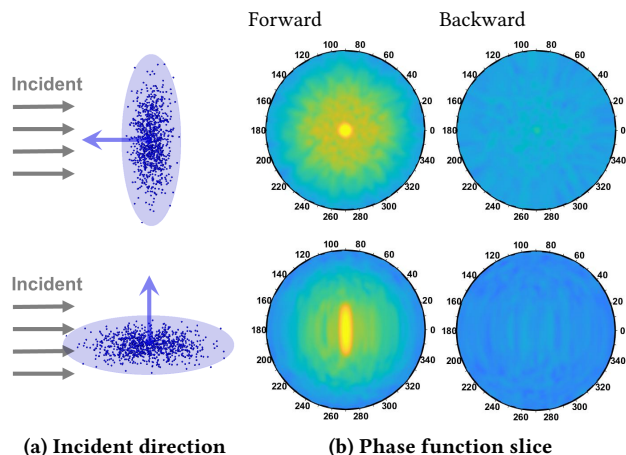


Fig. 11. Visualizations of slices $f_p(\hat{n}^{\text{inc}}, \cdot)$ of a phase function for two incident directions \hat{n}^{inc} at $\lambda = 700\text{nm}$. This phase function is computed using a configuration where 100 particles with radii 300nm follow an anisotropic Gaussian distribution.

electromagnetism), our technique models a translucent material as clusters of particles randomly distributed in embedding media. Our work generalizes the widely-used Lorenz-Mie theory for rigorously deriving optical properties of scattering media, and can be readily used in any radiative-based light transport simulator. We have demonstrated the significant effects of departing from the underlying assumptions of Lorenz-Mie theory, and the versatility for modeling a wide range of participating media by modifying the arrangement of particles within each cluster, including isotropic, anisotropic, and correlated media.

ACKNOWLEDGMENTS

We thank the anonymous reviewers for their comments and suggestions. Yu and Shuang are partially supported by NSF grant 1813553. Adrian is partially supported by the European Research Council (ERC) under the EU Horizon 2020 research and innovation programme (project CHAMELEON, grant No 682080), the EU MSCA-ITN programme (project PRIME, grant No 956585) and the Spanish Ministry of Science and Innovation (project PID2019-105004GB-I00).

REFERENCES

- Carlos Aliaga, Carlos Castillo, Diego Gutierrez, Miguel A Otaduy, Jorge Lopez-Moreno, and Adrian Jarabo. 2017. An appearance model for textile fibers. *Computer Graphics Forum* 36, 4 (2017), 35–45.
- Marco Ament, Christoph Bergmann, and Daniel Weiskopf. 2014. Refractive radiative transfer equation. *ACM Trans. Graph.* 33, 2 (2014), 1–22.
- Chen Bar, Marina Alterman, Ioannis Gkioulekas, and Anat Levin. 2019. A Monte Carlo framework for rendering speckle statistics in scattering media. *ACM Trans. Graph.* 38, 4 (2019), 1–22.
- Chen Bar, Ioannis Gkioulekas, and Anat Levin. 2020. Rendering near-field speckle statistics in scattering media. *ACM Trans. Graph.* 39, 6 (2020), 1–18.
- Laurent Belcour and Pascal Barla. 2017. A practical extension to microfacet theory for the modeling of varying iridescence. *ACM Trans. Graph.* 36, 4 (2017).
- Benedikt Bitterli, Srinath Ravichandran, Thomas Müller, Magnus Wrenninge, Jan Novák, Steve Marschner, and Wojciech Jarosz. 2018. A radiative transfer framework for non-exponential media. *ACM Trans. Graph.* 37, 6 (2018), 225.

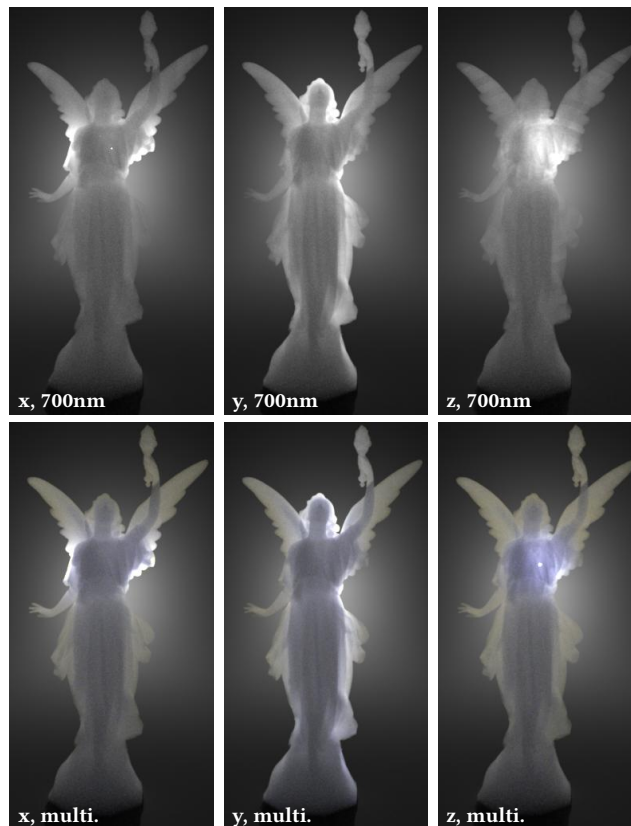


Fig. 12. Renderings of homogeneous Lucy models with the same anisotropic medium as in Figure 11. The medium’s orientation—which determines the axis of the disk—is aligned respectively with the x -, y -, and z -axis in the three columns, leading to distinctive appearances. We show single-wavelength ($\lambda = 700\text{nm}$) renderings on the top and multi-spectral ones on the bottom.

- Tom Cuypers, Tom Haber, Philippe Bekaert, Se Baek Oh, and Ramesh Raskar. 2012. Reflectance Model for Diffraction. *ACM Trans. Graph.* 31, 5 (2012).
- Zhao Dong, Bruce Walter, Steve Marschner, and Donald P Greenberg. 2015. Predicting appearance from measured microgeometry of metal surfaces. *ACM Trans. Graph.* 35, 1 (2015), 1–13.
- Amos Egel, Lorenzo Pattelli, Giacomo Mazzamuto, Diederik S Wiersma, and Uli Lemmer. 2017. CELES: CUDA-accelerated simulation of electromagnetic scattering by large ensembles of spheres. *Journal of Quantitative Spectroscopy and Radiative Transfer* 199 (2017), 103–110.
- Viggo Falster, Adrian Jarabo, and Jeppe Revall Frisvad. 2020. Computing the Bidirectional Scattering of a Microstructure Using Scalar Diffraction Theory and Path Tracing. *Computer Graphics Forum* 39, 7 (2020).
- Leslie L Foldy. 1945. The multiple scattering of waves. I. General theory of isotropic scattering by randomly distributed scatterers. *Physical review* 67, 3-4 (1945), 107.
- Jeppe Revall Frisvad, Niels Jørgen Christensen, and Henrik Wann Jensen. 2007. Computing the scattering properties of participating media using Lorenz-Mie theory. *ACM Trans. Graph.* 26, 3 (2007), 60–es.
- Jeppe Revall Frisvad, Søren Alkærsig Jensen, Jonas Skovlund Madsen, António Correia, Li Yang, Søren Kimmer Schou Gregersen, Youri Meuret, and P-E Hansen. 2020. Survey of models for acquiring the optical properties of translucent materials. *Computer Graphics Forum* 39, 2 (2020), 729–755.
- Ioannis Gkioulekas, Bei Xiao, Shuang Zhao, Edward H Adelson, Todd Zickler, and Kavita Bala. 2013. Understanding the role of phase function in translucent appearance. *ACM Trans. Graph.* 32, 5 (2013), 1–19.
- Werner J Glantschnig and Sow-Hsin Chen. 1981. Light scattering from water droplets in the geometrical optics approximation. *Applied Optics* 20, 14 (1981), 2499–2509.

